J|A|C|S ARTICLES

Published on Web 11/05/2009

Insights into the (Superoxo)Fe(III)Fe(III) Intermediate and Reaction Mechanism of *myo*-Inositol Oxygenase: DFT and ONIOM(DFT:MM) Study

Hajime Hirao and Keiji Morokuma*

Fukui Institute for Fundamental Chemistry, Kyoto University, 34-4 Takano Nishihiraki-cho, Sakyo, Kyoto 606-8103, Japan, and Cherry L. Emerson Center for Scientific Computation and Department of Chemistry, Emory University, Atlanta, Georgia 30322

Received June 27, 2009; E-mail: morokuma@fukui.kyoto-u.ac.jp

Abstract: The (superoxo)Fe(III)Fe(III) reactive species and the catalytic reaction mechanism of a diiron enzyme, *myo*-inositol oxygenase (MIOX), were theoretically investigated by means of density functional theory (DFT) and ONIOM quantum mechanical/molecular mechanical (QM/MM) approaches. The ground state of the (superoxo)Fe(III)Fe(III) intermediate was shown to have a side-on coordination geometry and an $S = 1/2$ spin state, wherein the two iron sites are antiferromagnetically coupled while the superoxide site and the nearest iron are ferromagnetically coupled. A full reaction pathway leading to a D-glucuronate product from *myo*-inositol was proposed based on ONIOM computational results. Two major roles of the enzyme surrounding during the catalytic reaction were identified. One is to facilitate the initial H-abstraction step, and the other is to restrict the movement of the substrate via H-bonding interactions in order to avoid unwanted side reactions. In our proposed mechanism, O−O bond cleavage has the highest barrier, thus constituting the rate-limiting step of the reaction. The unique role of the bridging hydroxide ligand as a catalytic base was also identified.

1. Introduction

myo-Inositol (MI) is a structural component of inositol phosphates and phosphoinositides that are known to serve as second messengers to mediate important cellular processes including insulin action.[1,2] Accumulated evidence indicates that depletion of the intracellular level of MI is associated with various diabetic complications such as nephropathy, retinopathy, neuropathy, and cataract.[3−6] MI is degraded via conversion to D-glucuronate (DG),[7] which is the first committed step in MI catabolism (Scheme 1).[8−10] This MI-to-DG oxidative conversion was found to proceed predominantly in the kidney catalyzed by a nonheme enzyme called *myo*-inositol oxygenase (MIOX),[11−13] and it was also shown that MIOX is expressed, albeit at much lower levels, in extra-renal tissues where diabetic complications occur.[12e] It is therefore conceivable that the MIOX function somehow regulates the MI level and thereby plays a critical role in the pathogenesis of diabetic complications. In support of this notion, a recent study conducted by Prabhu et al. demonstrated that depletion of MI is likely mediated by enhanced expression of MIOX.[12d] A correlation between increased MIOX activity and increased hypergycemia was also reported.[14] MIOX could thus be a potential therapeutic target in diabetic diseases, and therefore, a molecular level understanding of the enzyme is of paramount importance.

Scheme 1. MIOX-Catalyzed Conversion from MI to DG

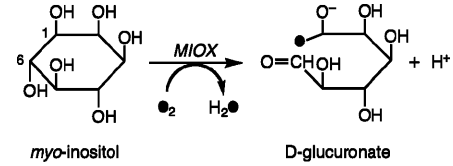

Despite the apparent biomedical and chemical significance of MIOX, its molecular details had long remained unclear, which prevented a full understanding of the catalytic mechanism

(1) Toker, A. *Cell. Mol. Life Sci.* **2002**, *59*, 761–779.
(2) Payrastre, B.; Missy, K.; Giuriato, S.; Bodin, S.; Plantavid, M.; Gratacap, M. P. *Cell. Signalling* **2001**, *13*, 377–387.
(3) Winegrad, A. I. *Diabetes* **1987**, *36*, 396–406.
(4) Arner, R. J.; Prabhu, K. S.; Thompson, J. T.; Hildenbrandt, G. R.; Liken, A. D.; Reddy, C. C. *Biochem. J.* **2001**, *360*, 313–320.
(5) Sundkvist, G.; Dahlin, L.-B.; Nilsson, H.; Eriksson, K.-F.; Lindgärde, F.; Rosén, I.; Lattimer, S. A.; Sima, A. A. F.; Sullivan, K.; Greene, D. A. *Diabetic Med.* **2000**, *17*, 259–268.
(6) Head, K. A. *Altern. Med. Rev.* **2006**, *11*, 294–329.
(7) Charalampous, F. C.; Lyras, C. *J. Biol. Chem.* **1957**, *228*, 1–13.
(8) Hankes, L. V.; Politzer, W. M.; Touster, O.; Anderson, L. *Ann. N.Y. Acad. Sci.* **1969**, *165*, 564–576.
(9) Charalampous, F. C. *J. Biol. Chem.* **1960**, *235*, 1286–1291.
(10) Moskala, R.; Reddy, C. C.; Minard, R. D.; Hamilton, G. A. *Biochem. Biophys. Res. Commun.* **1981**, *99*, 107–113.
(11) Charalampous, F. C. *J. Biol. Chem.* **1959**, *234*, 220–227.
(12) (a) Reddy, C. C.; Swan, J. S.; Hamilton, G. A. *J. Biol. Chem.* **1981**, *256*, 8510–8518. (b) Reddy, C. C.; Pierzchala, P. A.; Hamilton, G. A. *J. Biol. Chem.* **1981**, *256*, 8519–8524. (c) Arner, R. J.; Prabhu, K. S.; Reddy, C. C. *Biochem. Biophys. Res. Commun.* **2004**, *324*, 1386–1392. (d) Prabhu, K. S.; Arner, R. J.; Vunta, H.; Reddy, C. C. *J. Biol. Chem.* **2005**, *280*, 19895–19901. (e) Arner, R. J.; Prabhu, K. S.; Krishnan, V.; Johnson, M. C.; Reddy, C. C. *Biochem. Biophys. Res. Commun.* **2006**, *339*, 816–820.
(13) (a) Bollinger, J. M., Jr.; Krebs, C. *Curr. Opin. Chem. Biol* **2007**, *11*, 151–158. (b) Bollinger, J. M., Jr.; Diao, Y.; Matthews, M. L.; Xing, G.; Krebs, C. *Dalton Trans.* **2009**, 905–914.
(14) Nayak, B.; Xie, P.; Akagi, S.; Yang, Q.; Sun, L.; Wada, J.; Thakur, A.; Danesh, F. R.; Chugh, S. S.; Kanwar, Y. S. *Proc. Natl. Acad. Sci. U.S.A.* **2005**, *102*, 17952–17957.

10.1021/ja905296w CCC: $40.75

operating in the enzyme. A series of recent experiments, however, provided exciting breakthroughs in the knowledge of MIOX, demonstrating, for example, that it contains a coupled dinuclear iron cluster. Spectroscopic analysis done by Xing et al. showed that MIOX utilizes a mixed-valence Fe(II)Fe(III) intermediate (**1**) to activate O_2.[15] Furthermore, their subsequent spectroscopic and kinetic analyses showed that an early step of the MIOX reaction is associated with a kinetic isotope effect of 5 or even larger and that the dioxygen binding to MIOX is reversible.[16] These results led them to conclude that a hydrogen atom is abstracted from the substrate by a (superoxo)Fe(II-I)Fe(III) intermediate (**2**) that is generated upon O_2 binding to **1**. This mechanism is very intriguing, since for many of the previously characterized nonheme and heme iron enzymes, high-valence iron intermediates have been invoked as key species responsible for H-abstraction.[17] For example, in taurine:α-ketoglutarate dioxygenase (TauD), an oxo-iron(IV) species was identified as the reactive species for H-abstraction.[18] Analogous ferryl intermediates ligated by a porphyrin π-cation radical, collectively known as compound I (Cpd I) in heme enzymes, are also considered the most probable reactive species in cytochromes P450.[19,20] Moreover, there is evidence that soluble methane monooxygenase (sMMO) utilizes a diiron(IV/IV) complex (**Q**) to cleave a C−H bond of methane, and the R2 subunit of ribonuclease reductase (RNR-R2) oxidizes a tyrosine residue by use of a diiron(III/IV) complex (**X**).[21] By comparison, examples of metalloenzymes that use superoxo-ferric species as reactive species to effect C−H cleavage are still scarce.[13a] Isopenicillin *N* synthase (IPNS)[22,23] and possibly (*S*)-2-hydroxypropylphosphonic acid epoxidase (HppE),[24] as well as MIOX, represent rare examples of such nonheme enzymes. The use of a superoxo-ferric reactive species was also proposed, although not for C−H cleavage, in heme dioxygenases called indoleamine 2,3-dioxygenase (IDO) and tryptophan 2,3-dioxygenase (TDO).[25] In view of their capability to permit unique catalytic processes such as four-electron oxidation and dioxygenation, superoxo-ferric intermediates warrant greater scrutiny.

Scheme 2. Initial Steps of the MIOX Catalytic Cycle

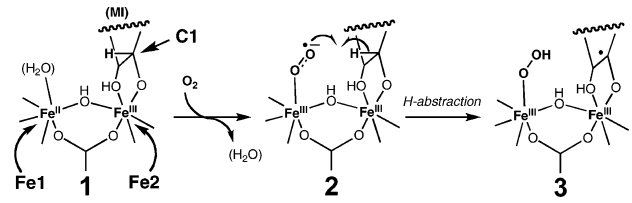

Recently, Brown et al.[26] and Thorsell et al.[27] undertook X-ray crystallographic studies, which provided valuable insights into the three-dimensional structure of MIOX. These studies revealed that the overall structure of MIOX bears no obvious similarity to that of sMMO or RNR-R2. MIOX also exhibited clear distinction in the active site structure as compared to sMMO and RNR-R2. Whereas sMMO and RNR-R2 have four carboxylate residues (Asp or Glu) and two histidines around the two irons, MIOX has two aspartates and four histidines that build up the cluster. Remarkably, the MI substrate was bound in a bidentate manner to only one of the two iron atoms through the hydroxyl groups on C1 and C6 of MI, with the remaining hydroxyl groups stably anchored by the interactions with hydrogen-bond donors and acceptors from the surrounding amino acid residues.

A plausible mechanism for the initial stage of the MIOX reaction, based on the recent experimental findings, is described in Scheme 2. In this mechanism, dioxygen binding to the Fe(II) site (Fe1) of the mixed-valence intermediate **1** takes place first to generate a (superoxo)Fe(III)Fe(III) reactive species **2**. The superoxide part of **2** then abstracts a hydrogen atom from the C1 of the MI substrate that is bound to Fe2. An FeOOH-type intermediate **3** is then supposedly generated as a result of H-abstraction.

A great deal of work still remains to be done to fully understand the catalytic mechanism of MIOX. In particular, the nature of reactive species **2** and the mechanism of its reaction are yet to be elucidated. In this challenging endeavor, multilayered quantum mechanical and molecular mechanical (QM/MM) methods such as the ONIOM method can make significant contributions. We thus addressed these issues using density functional theory (DFT) and ONIOM(DFT:MM) computational approaches. DFT is a standard method used to identify the intrinsic electronic and structural properties of metalloenzymes. The ONIOM approach has emerged as a promising tool that allows for the analysis of large molecules including metalloenzymes, with the effect of enzyme surrounding on the active-site properties adequately taken into account.

2. Method

2.1. Protein Setup and MM Parameters. An X-ray structure of mouse MIOX (PDB code 2HUO, 2.00 Å resolution)[26] was used as a starting point for our DFT and ONIOM calculations. Hydrogen atoms of all the amino acid residues as well as the missing atoms in Phe28, Lys45, and Glu265 were added to the 2HUO structure

(15) (a) Xing, G.; Hoffart, L. M.; Diao, Y.; Prabhu, K. S.; Arner, R. J.; Reddy, C. C.; Krebs, C.; Bollinger, J. M., Jr. *Biochemistry* **2006**, *45*, 5393–5401. (b) Xing, G.; Barr, E. W.; Diao, Y.; Hoffart, L. M.; Prabhu, K. S.; Arner, R. J.; Reddy, C. C.; Krebs, C.; Bollinger, J. M., Jr. *Biochemistry* **2006**, *45*, 5402–5412.
(16) Xing, G.; Diao, Y.; Hoffart, L. M.; Barr, E. W.; Prabhu, K. S.; Arner, R. J.; Reddy, C. C.; Krebs, C.; Bollinger, J. M., Jr. *Proc. Natl. Acad. Sci. U.S.A.* **2006**, *103*, 6130–6135.
(17) Krebs, C.; Fujimori, D. G.; Walsh, C. T.; Bollinger, J. M., Jr. *Acc. Chem. Res.* **2007**, *40*, 484–492.
(18) (a) Price, J. C.; Barr, E. W.; Tirupati, B.; Bollinger, J. M., Jr.; Krebs, C. *Biochemistry* **2003**, *42*, 7497–7508. (b) Price, J. C.; Barr, E. W.; Glass, T. E.; Krebs, C.; Bollinger, J. M., Jr. *J. Am. Chem. Soc.* **2003**, *125*, 13008–13009. (c) Riggs-Gelasco, P. J.; Price, J. C.; Guyer, R. B.; Brehm, J. H.; Barr, E. W.; Bollinger, J. M., Jr.; Krebs, C. *J. Am. Chem. Soc.* **2004**, *126*, 8108–8109.
(19) Denisov, I. G.; Makris, T. M.; Sligar, S. G.; Schlichting, I. *Chem. Rev.* **2005**, *105*, 2253–2277.
(20) (a) Shaik, S.; Kumar, D.; de Visser, S. P.; Altun, A.; Thiel, W. *Chem. Rev.* **2005**, *105*, 2279–2328. (b) Shaik, S.; Hirao, H.; Kumar, D. *Acc. Chem. Res.* **2007**, *40*, 532–542. (c) Shaik, S.; Hirao, H.; Kumar, D. *Nat. Prod. Rep.* **2007**, *24*, 533–552.
(21) (a) Wallar, B. J.; Lipscomb, J. D. *Chem. Rev.* **1996**, *96*, 2625–2657. (b) Bollinger, J. M., Jr.; Krebs, C. *J. Inorg. Biochem.* **2006**, *100*, 586–605.
(22) Roach, P. L.; Clifton, I. J.; Hensgens, C. M. H.; Shibata, N.; Schofield, C. J.; Hajdu, J.; Baldwin, J. E. *Nature* **1997**, *387*, 827–830.
(23) (a) Lundberg, M.; Morokuma, K. *J. Phys. Chem. B* **2007**, *111*, 9380–9389. (b) Lundberg, M.; Siegbahn, P. E. M.; Morokuma, K. *Biochemistry* **2008**, *47*, 1031–1042.
(24) Yan, F.; Munos, J. W.; Liu, P.; Liu, H. W. *Biochemistry* **2006**, *45*, 11473–11481.
(25) Chung, L. W.; Li, X.; Sugimoto, H.; Shiro, Y.; Morokuma, K. *J. Am. Chem. Soc.* **2008**, *130*, 12299–12309.
(26) Brown, P. M.; Caradoc-Davies, T. T.; Dickson, J. M. J.; Cooper, G. J. S.; Loomes, K. M.; Baker, E. N. *Proc. Natl. Acad. Sci. U.S.A.* **2006**, *103*, 15032–15037.
(27) Thorsell, A. G.; Persson, C.; Voevodskaya, N.; Busam, R. D.; Hammarström, M.; Gräslund, S.; Gräslund, A.; Hallberg, B. M. *J. Biol. Chem.* **2008**, *283*, 15209–15216.

using VMD.[28] A few of the newly added hydrogen atoms had unusual bond angles, and these were manually adjusted. The protonation states of histidine residues were determined as follows with PROPKA[29] analysis and visual inspection: HIE48, HID50, HID98, HIE110, HIE117, HID123, HID182, HID194, HID220, and HIE226, where HID and HIE stand for neutral histidines with protonated $N_{\delta 1}$ and $N_{\epsilon 2}$ atoms, respectively. The PDB file contained a formate ion, for which RESP atomic charges were derived at the HF/6-31G* level with Gaussian Development Version[30] and the RED script.[31] The charges (Q) for the formate thus obtained are $Q(O) = -0.814623$; $Q(C) = 0.818689$; $Q(H) = -0.189443$. Also, the H5 and O2 atom types were used for the hydrogen and oxygen atoms, respectively, and parameters for the H−C bond ($K_r = 367.0$ kcal/(mol Å^2), $r_{eq} = 1.08$ Å) and the H−C−O angle ($K_\theta = 50.0°$, $\theta_{eq} = 119.0$ kcal/(mol deg^2) were taken from those for formic acid in parm99.dat.[32] The van der Waals parameters for Fe optimized specifically for dinuclear iron enzymes were used here ($R = 1.4560$ Å, $\varepsilon = 0.0130$ kcal/mol).[33] The bridging oxygen (O_x) between the two Fe atoms was treated as hydroxide (OH^-) based on the reasonable assumption made by Brown et al.[26] The "OH" and "HO" AMBER atom types were assigned to the oxygen and hydrogen atoms in the hydroxide, respectively. The "CT", "OH", "H1", and "HO" atom types were used for the carbon, oxygen, aliphatic hydrogen, and hydroxyl hydrogen atoms in MI, respectively. The hydroxyl group on C1 of MI was treated as ionized, while the other hydroxyl groups were assumed to be neutral.[26] The Merz−Kollman (MK) electrostatic potential (ESP) charges[34] obtained with basis set B1 for an active-site model without O_2 ($S = 1/2$, with antiferromagnetically coupled high spin irons) were used for the QM atoms in ONIOM low-real system calculations (see Table S1 in Supporting Information). The atomic charges of the oxygen atoms in O_2 were assumed to be zero.[23a] An atomic radius of 0.785 Å was assumed for the Fe atoms when calculating their MK-ESP charges. The charges of the C_α atoms at the QM-MM boundary were adjusted so that both the model and real systems have integer charges in the ONIOM MM calculations. More specifically, the charge of C_α for a certain residue in the QM region (e.g., His98) was modified so that the backbone part of that residue possesses a zero charge. The MK charge of the link (hydrogen) atom was then added to the charge of C_α. For MM calculations, the AMBER force field[35] (from "parm96.dat") was used for most of the atoms, and the TIP3P model[36] was used for water molecules.

2.2. Preparatory MM Calculations. To obtain a good initial geometry for ONIOM calculations, a series of constrained AMBER-MM optimizations were performed starting with the 2HUO geometry. The hydrogen atoms, crystallographic waters, backbone atoms, and the atoms in the MM region were sequentially released in optimizations, while the active-site atoms (see below) were kept fixed throughout.

2.3. Models of the (Superoxo)Fe(III)Fe(III) Species. By replacing the Wat305 on Fe1 with O_2, two different calculation models of the (superoxo)Fe(III)Fe(III) intermediate, Model-AS and Model-ALL, were built (Figure 1). Model-AS is an active-site model for pure QM-DFT calculations. In this model, the side chains (from C_β onward) of two aspartates (Asp124, Asp253) and four histidines (His98, His123, His194, His220), the bridging hydroxide, O_2, MI, and two iron atoms (Fe1 and Fe2 in Scheme 2 and Figure 1) were included. The C_β atoms of the six residues were treated as methyl groups. The C_β atoms in Model-AS were frozen at the corresponding positions in the X-ray geometry to avoid a drastic geometric change. In Model-ALL, the QM-MM boundary cuts across the C_α−C_β bonds of these six residues, and hydrogen link atoms were added to the C_β methylene groups to satisfy valency. Thus, Model-AS and Model-ALL share the same QM atoms. In Model-ALL, all amino acid residues in 2HUO and crystallographic water molecules were included. The total charges of the QM region and the whole system were 1 and −10, respectively. In another PDB structure of mouse MIOX (3BXD),[27] a crystallographic water molecule (Wat375) is present near Asp253 in the active site but not in 2HUO. This water molecule was added to Model-ALL. Wat375 could thus be viewed as Wat305 displaced from Fe1 by O_2. Model-AS and Model-ALL contained 91 and 4617 atoms, respectively.

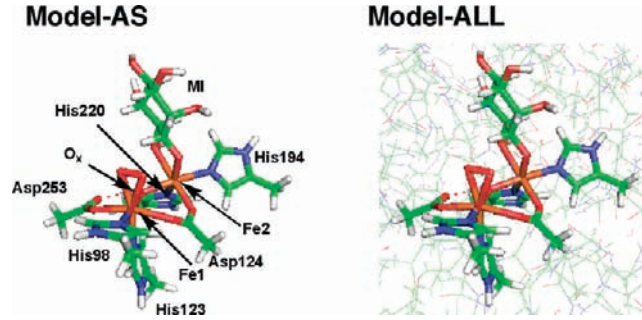

Figure 1. Models for the calculations. Model-AS and Model-ALL contain 91 and 4617 atoms (with 91 QM atoms including link H atoms), respectively. In Model-ALL, only MM atoms near the active site are shown here. PyMol was used to draw the molecules.[37]

2.4. DFT and ONIOM Calculations. Broken-symmetry DFT calculations were performed for Model-AS and for the QM region of Model-ALL with the B3LYP functional[38] in conjunction with two different basis sets B1 and B2. B1 is a combination of the SDD effective core potential basis set for Fe and the 6-31G* basis set for the rest of the atoms and was used for geometry optimizations. The TZVP basis set (B2) was used for single point calculations to improve energetics. The entire enzyme (Model-ALL) was treated by the ONIOM(B3LYP:AMBER) method.[39] In the ONIOM method, the total energy is extrapolated from the energies obtained by a set of less expensive calculations. If QM (high-level) and MM (low-level) layers are used, the total energy (E^{ONIOM}) may be calculated by

$$E^{ONIOM} = E^{real,MM} + E^{model,QM} - E^{model,MM} \quad (1)$$

where $E^{real,MM}$ is the energy of the real (large) system calculated by MM, $E^{model,QM}$ is the energy of the model (small) system

(28) Humphrey, W.; Dalke, A.; Schulten, K. *J. Mol. Graphics* **1996**, *14*, 33–38.
(29) (a) Li, H.; Robertson, A. D.; Jensen, J. H. *Proteins* **2005**, *61*, 704–721. (b) Bas, D. C.; Rogers, D. M.; Jensen, J. H. *Proteins* **2008**, *73*, 765–783.
(30) Frisch, M. J.; et al. *Gaussian Development Version*, Revision G.03; Gaussian, Inc: Wallingford CT, 2008.
(31) Pigache, A.; Cieplak, A. P.; Dupradeau, F.-Y. 227th ACS National Meeting, Anaheim, CA, USA, March 28−April 1, 2004.
(32) Wang, J.; Cieplak, P.; Kollman, P. A. *J. Comput. Chem.* **2000**, *21*, 1049–1074.
(33) Khavrutsukii, I. V. Dissertation, Emory University 2006, Chapter 6.
(34) Besler, B. H.; Merz, K. M.; Kollman, P. A. *J. Comput. Chem.* **1990**, *11*, 431–439.
(35) Cornell, W. D.; Cieplak, P.; Bayly, C. I.; Gould, I. R.; Merz, K. M., Jr.; Ferguson, D. M.; Spellmeyer, D. C.; Fox, T.; Caldwell, J. W.; Kollman, P. A. *J. Am. Chem. Soc.* **1995**, *117*, 5179–5197.
(36) Jorgensen, W. L.; Chandrasekhar, J.; Madura, J. D.; Impey, R. W.; Klein, M. L. *J. Chem. Phys.* **1983**, *79*, 926–935.
(37) DeLano, W. L. *The PyMOL Molecular Graphics System*; DeLano Scientific: San Carlos, CA, 2002.
(38) Becke, A. D. *J. Chem. Phys.* **1993**, *98*, 5648–5652. (b) Lee, C.; Yang, W.; Parr, R. G. *Phys. Rev. B* **1988**, *37*, 785–789. (c) Vosko, S. H.; Wilk, L.; Nusair, M. *Can. J. Phys.* **1980**, *58*, 1200–1211.
(39) (a) Maseras, F.; Morokuma, K. *J. Comput. Chem.* **1995**, *16*, 1170–1179. (b) Svensson, M.; Humbel, S.; Froese, R. D. J.; Matsubara, T.; Sieber, S.; Morokuma, K. *J. Phys. Chem.* **1996**, *100*, 19357–19363. (c) Dapprich, S.; Komáromi, I.; Byun, K. S.; Morokuma, K.; Frisch, M. J. *J. Mol. Struct. (THEOCHEM)* **1999**, *461−462*, 1–21. (d) Vreven, T.; Byun, K. S.; Komáromi, I.; Dapprich, S.; Montgomery, J. A., Jr.; Morokuma, K.; Frisch, M. J. *J. Chem. Theory Comput.* **2006**, *2*, 815–826. (e) Lundberg, M.; Kawatsu, T.; Vreven, T.; Frisch, M. J.; Morokuma, K. *J. Chem. Theory Comput.* **2009**, *5*, 222–234.

Table 1. RMSD Values (in Å) of the Optimized Structures and the X-ray Structure of the Oxidized Form of **1**

	rmsd(all)[a]	rmsd(as)[b]
Model-AS		0.40
Model-ALL (ME-opt)	0.89	0.26
Model-ALL (EE-opt)	0.89	0.25

[a] rmsd for all heavy atoms, with crystallographic waters (other than Wat305 over Fe1), formate ion, and the missing atoms in the PDB file excluded. [b] rmsd for the heavy atoms in the active site.

calculated by QM, and $E^{\text{model,MM}}$ is the energy of the model (small) system calculated by MM. Two different ONIOM methods were applied to Model-ALL: (1) ONIOM-ME (mechanical embedding), in which the electrostatic interactions between the QM and MM atoms are described classically using the MK-ESP charges of the QM part calculated at the isolated geometry (see section 2.1), and (2) ONIOM-EE (electronic embedding), which allows the QM wave function to polarize under the influence of the point charges of the surrounding MM atoms. Because of the high computational demands, ONIOM-ME harmonic frequencies for the entire Model-ALL system were calculated only for key ONIOM-ME optimized geometries to derive information used for zero-point energy (ZPE) and free energy calculations.

Our calculation of a reaction profile is concerned with energy variation along a certain reaction coordinate. However, it is known that a conformational change of some molecule or residue occurring far from the reaction center sometimes causes a decrease in total energy, which is obviously not associated with the reaction of interest. To avoid this artificial energy drop, geometry optimizations were repeated a few times for the first H-abstraction step. Repetition of this calculation for all neighboring intermediate pairs is prohibitively demanding and was therefore not done. Nevertheless, the rigid nature of the active site of MIOX ensures that the risk of the artifact is not as high as in other flexible enzymes.

3. Results and Discussion

3.1. Assessment of the Quality of Computationally Derived Geometries. The X-ray structure of mouse MIOX corresponds to a water-bound Fe(III)Fe(III) state, which is an oxidized form of **1**. To begin with, we optimized the geometry of this state using Model-AS and Model-ALL, to assess how well theory predicts the enzyme geometry. Antiferromagnetically coupled sextet spin states (total spin $S = 0$) were assumed for the two iron ions.[15] Table 1 summarizes the root-mean-square deviation (rmsd) values for the calculated geometries relative to the X-ray geometry; rmsd(all) in the table is for all heavy atoms, and rmsd(as) is for the heavy atoms in the active site only. As can be seen from Table 1, ONIOM-ME yielded an rmsd(all) value as small as 0.89 Å. In fact, in the superposition of the theoretical and crystal geometries given in Figure 2a, one sees excellent agreement of the geometries. rmsd(as) obtained with Model-AS was 0.40 Å, where the small value is apparently in part due to the geometric constraints imposed on the C_β atoms. Despite the fact that the geometric constraints were removed in the ONIOM-ME optimization, the rmsd(as) value was even smaller (0.26 Å) than that in Model-AS (Table 1 and Figure 2b). Further inspection revealed that the larger deviation of the active-site atoms in Model-AS comes from the lack of H-bonding interactions of MI with nearby residues, and thus, the substrate is not anchored at a suitable position. ONIOM-EE optimization did not result in a significant change in the rmsd(all) and rmsd(as) values compared to those obtained by ONIOM-ME; therefore, we decided to use more expensive ONIOM-EE calculations only for single-point energy evaluations in subsequent calculations. For comparison, we note that

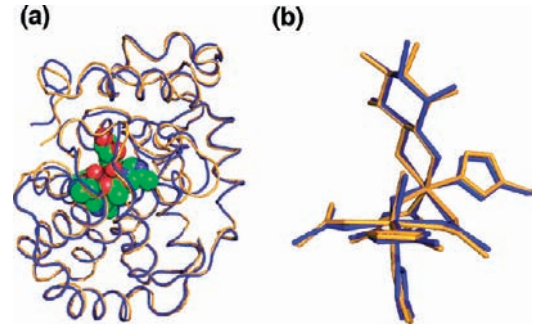

Figure 2. Superposition of the X-ray (blue) and ONIOM-ME optimized (orange) geometries: (a) all heavy atoms (ribbon representation) and (b) active-site heavy atoms (stick representation).

Scheme 3. Formal Spin States Considered for the Two Iron Atoms (Fe1 and Fe2, see Scheme 4) and the $O_2^{\bullet-}$ Moiety of **2**[a]

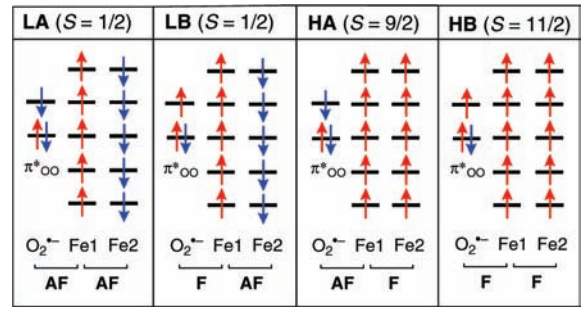

[a] "A" and "AF" stand for ferromagnetic and antiferromagnetic coupling, respectively.[42]

in a previous study on glutathione peroxidase (GPx), rmsd(all) values were 1.71−1.73 Å, whereas rmsd(as) values were 0.79−1.17 Å in ONIOM(DFT:MM) calculations and 1.48−2.26 Å in active-site only calculations.[40] The remarkably smaller rmsd values obtained here underscore the excellent agreement between the calculated and X-ray structures in the present system. There seem to be several reasons for the smaller rmsd values for MIOX compared with those for GPx. First, all crystallographic water molecules in the PDB file were included in our calculations, whereas for GPx, water coordinates were not available because of the low resolution (2.9 Å) of the X-ray structure. Indeed, in the study of GPx, the deviations of the active-site atoms were significantly reduced when two key water molecules were included.[40] The crystallographic water molecules are thus likely to play key roles in maintaining enzyme structure. In addition, unlike MIOX (monomer), GPx is a tetramer; therefore, a large deviation may arise if only one of the chains is used for calculations as the contributions of other chains are then neglected. The less flexible active site in MIOX compared with that in GPx could also be a possible reason for the smaller rmsd values obtained for the active site in the calculations of MIOX.

3.2. (Superoxo)Fe(III)Fe(III) Intermediate. We now discuss the (superoxo)Fe(III)Fe(III) intermediate **2**, which is arguably the reactive species of MIOX. The relative stability of four spin states (**LA**, **LB**, **HA**, and **HB** in Scheme 3) of **2** in both side-on and end-on O_2 coordination geometries (Scheme 4) was evaluated. In all spin states, the superoxide site formally has an unpaired electron, while each of the two iron sites has five unpaired electrons. Note, however, that the spin coupling patterns of the three sites are different. Since the superoxide

(40) Prabhakar, R.; Musaev, D. G.; Khavrutskii, I. V.; Morokuma, K. *J. Phys. Chem. B* **2004**, *108*, 12643–12645.

Scheme 4. Side-On and End-On Coordination Geometries of **2**

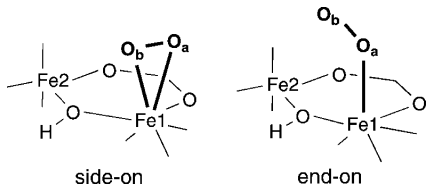

Table 2. Relative Energies (in kcal/mol, without ZPE correction) of Different Coordination and Spin States of **2** (see Schemes 3 and 4)[a]

state	Model-AS DFT (B2//B1)	Model-ALL ONIOM-ME[b] (B2//B1)	Model-ALL ONIOM-EE[c] (B2) //ME(B1)
LA (side-on)	5.1 (4.8)	4.9 (4.7)	4.6 (4.4)
LA (end-on)	7.9 (8.1)	9.2 (10.1)	9.6 (10.5)
LB (side-on)	0.0 (0.0)	0.0 (0.0)	0.0 (0.0)
LB (end-on)	N/A[d]	N/A[d]	N/A[d]
HA (side-on)	6.7 (6.7)	6.6 (6.6)	6.2 (6.2)
HA (end-on)	9.2 (9.7)	10.4 (11.4)	10.9 (11.9)
HB (side-on)	1.8 (1.9)	1.5 (1.7)	1.3 (1.5)
HB (end-on)	N/A[d]	N/A[d]	N/A[d]

[a] Energies with dispersion correction are in parentheses. [b] Mechanical embedding. [c] Electronic embedding. [d] Geometry optimization resulted in dissociation of O_2.

site and the Fe2 site are distant from each other, coupling between these sites will be negligible. Table 2 lists the relative energies of **2** obtained using several methods. In each spin state, a preference for the side-on geometry is observed. Further, the lower energies of **LB** and **HB** compared with **LA** and **HA** signify that the Fe1 and the superoxide site favor ferromagnetic coupling. Consistent with the spin state identified by spectroscopic analysis ($S = 1/2$),[16] **LB** was the most stable irrespective of the method used (Table 2). Although **LA** also has $S = 1/2$, **LB** was favored in all calculations. We therefore predict that **LB** with a side-on coordination geometry is the ground state of **2**, in which high-spin iron ions are antiferromagnetically coupled.[41] Our calculations also suggest that the relative energy increases in the following order: **LB** < **HB** < **LA** < **HA**.

Since conventional DFT is not capable of describing dispersion interactions properly, we separately estimated the dispersion correction (E_{disp}) for each state applying the formula proposed by Grimme:[43]

$$E_{\mathrm{disp}} = -s_6 \sum_{i=1}^{N-1} \sum_{j=i+1}^{N} \frac{C_6^{ij}}{R_{ij}^6} f(R_{ij}) \qquad (2)$$

where s_6 is a global scaling factor (1.05 for B3LYP), C_6^{ij} is a dispersion coefficient, R_{ij} is the internuclear distance, and $f(R_{ij})$ is a damping function. This method was applied to the QM atoms in single point calculations to analyze the effect of dispersion on the relative stability of spin states. It turned out that the dispersion corrections do not change the relative energies significantly nor do they alter the spin-state ordering (see values in parentheses in Table 2). Thus, the effect of dispersion on the relative stability is small in this particular case.

(41) Trials to find other more stable states having low-spin iron sites never succeeded.
(42) To facilitate our understanding of spin-coupling with respect to Fe1, the sign of electron spin on Fe1 was assumed positive in all cases. Note that the calculated spin density values actually have opposite signs in **LA** (see, for example, Table S2b in Supporting Information).
(43) Grimme, S. *J. Comput. Chem.* **2006**, *27*, 1787–1799.

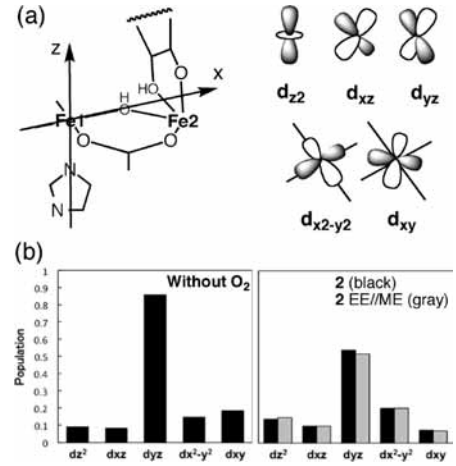

Figure 3. (a) Coordinate system and d-AOs. (b) Change in Fe1 β d-AO populations from the penta-coordinated state (left) to the O_2-bound state (**2**) in **LB** (right).

Scheme 5. Schematic Illustration of Superoxide Formation over Fe1

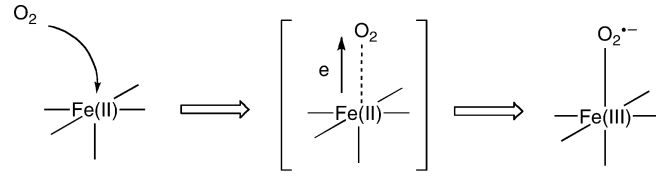

In the process of superoxo-iron(III) formation, dioxygen is supposed to bind to the Fe(II) center (Fe1), and then one electron has to be shifted from the iron center to dioxygen (Scheme 5). To better understand this process, we analyzed the spin population of d-AOs on the Fe1 center (Figure 3a), which was obtained at the ONIOM(B3LYP/B1:AMBER)-ME level. In Figure 3b, populations of the vacant spin (β) d orbitals in the O_2-unbound state as well as in the **LB** state of species **2** are shown.[44] d-AO populations were calculated from the sum of the populations in all three d-basis functions in B1. In the O_2-unbound state, namely, the pentacoordinate ferrous state, d-AO β populations are nearly zero except in the case of d_{yz}, indicating that d_{yz}-type orbital is doubly occupied while the other orbitals are only singly occupied (Figure 3b). Upon O_2-binding, the d_{yz}-AO β population significantly decreased in **2** (Figure 3b, right). This means that the charge transfer (CT) from Fe1 to O_2 takes place via the d_{yz} orbital. Consideration of orbital symmetry enables us to identify the π_y^* orbital of O_2 as the electron-accepting orbital. In the end-on geometry, CT via d_{yz} is less efficient because of smaller orbital overlap, which seems to be a reason the side-on geometry is preferred in **2**. After O_2 binding, however, the d_{yz}-AO β population did not decrease to zero, but there remained some amount of electron population (Figure 3b, right). This indicates that the number of electrons that shifted from Fe1 to O_2 is smaller than 1, as opposed to the schematic figure in Scheme 5, and the CT is thus not complete. In other words, *the resultant O_2-bound species **2** does not necessarily develop a "full" superoxide state, but it is better described as a "partial" (superoxo)Fe(III)Fe(III) species.*

This conclusion is confirmed by an atomic spin density analysis shown in Figure 4. The spin populations on the O_2 moiety of **2** in the **LA** and **HA** states were −0.55, while those in **LB** and **HB** were 1.57. It should be noted here that **LA** and **HA** can be viewed as states generated from the mixed-valence

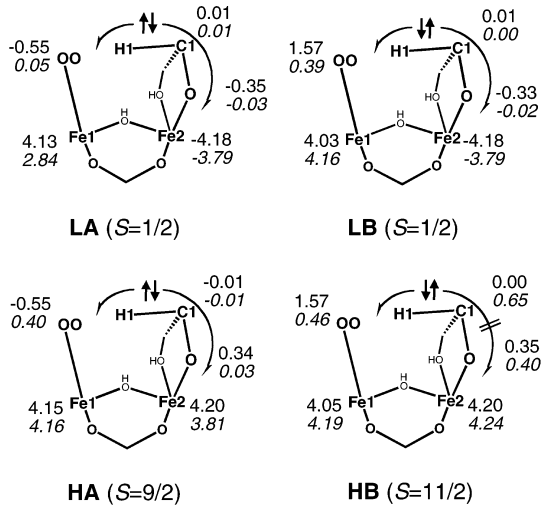

Figure 4. Key spin populations in **2** side-on (plain) and **3** (italic) obtained for Model-ALL with B1. Arrows depict the electron migration on going from **2** to **3**.

Fe(II)Fe(III) state **1** and singlet O_2 (spin population = 0), while **LB** and **HB** from **1** and triplet O_2 (spin population = 2). Accordingly, the number of electrons shifted from Fe1 to O_2 may be estimated by $|\rho(O_a) + \rho(O_b)|$ in **LA** and **HA**, and by $|2 - \rho(O_a) - \rho(O_b)|$ in **LB** and **HB**. In all cases, however, the values were 0.55 or 0.43, significantly smaller than 1 expected for complete charge transfer and superoxide formation. It appears therefore that the CT from Fe1 to O_2 is not complete.

3.3. Mechanism of the Catalytic Reaction. Most likely, the reaction of **2** starts with H-abstraction from the C1 of MI substrate.[16] Visual inspection of the geometries of **2** did not raise the possibility that other aliphatic hydrogen atoms could be abstracted. In Figure 5, the geometric change during H-abstraction is shown. Following the reaction path computationally, we found that H-abstraction from MI in **2** leads via transition state $\mathbf{TS_{2-3}}$ to FeOOH intermediate **3**. As discussed earlier, **LB** (side-on) is the ground state, and thus the reaction starts from this state (Figure 5a). At an early stage of the H-abstraction process, the side-on geometry changes smoothly to the end-on geometry that is more suitable for abstracting a hydrogen atom from the substrate. Indeed, as can be seen in Figure 5b, the superoxide part of $\mathbf{TS_{2-3}}$ has an end-on geometry, in which the distal oxygen (O_b) is placed in the vicinity of the C1 hydrogen (H1). Notably, at $\mathbf{TS_{2-3}}$, the O−O bond over Fe1 and the C−O bond over Fe2 are beautifully aligned, so the active-site geometry is well suited to this kind of H-abstraction. Immediately after H-abstraction, the OH part of FeOOH rotates about the O−O bond to form a H-bond with the oxygen (O_x) of the bridging hydroxide (Figure 5c).

It is interesting to see how the electrons are reorganized in the H-abstraction step (Figure S1 in Supporting Information). In the H-abstraction process from **2** to **3**, a proton along with one of the two electrons in the C−H bond migrates to the O_2 moiety to make a new O−H bond. As a result, the remaining electron in the C−H bond would be localized on the C1 center (Scheme 2). To examine the validity of this hypothesis, spin density distribution in intermediate **3** was analyzed (see Figure 4). It turned out that the electron left behind does not remain on C1 but is transferred to the Fe2−O moiety. Consequently, the spin population on C1 was zero even for **3** in **LA**, **LB**, and **HA**. This occurs because the electron spins on C1 and Fe2−O are antiparallel, which favorably form a bonding pair to eliminate the radical center and stabilize the system (Figure S1 in Supporting Information). **HB** is an exception, as spin localization does occur. The reason for this is that favorable electron pairing cannot occur because the electron spins on C1 and Fe2 are parallel (Figure S1 in Supporting Information). Such spin localization, however, would not have a beneficial effect on the stability of the system because the two sites repel each other as a result of Pauli repulsion. The electron migration pattern in **LA** could also lead to such an unfavorable situation; however, the problem is circumvented in this case by electron reorganization to produce a lower spin state on Fe1 (Figure S1 in Supporting Information).

In the reaction profile obtained with Model-ALL (Figure 6), the barrier for H-abstraction is seen to be 17.7 kcal/mol in **LB** with zero-point energy (ZPE) correction. **HA** was also almost equally stable at $\mathbf{TS_{2-3}}$. This barrier height is comparable to that for cytochrome $P450_{cam}$ compound I (~20 kcal/mol), as obtained with a QM/MM method,[45] and this theoretically verifies the ability of **2** to effect C−H cleavage. To highlight the effect of the protein surrounding on the H-abstraction step, the H-abstraction barriers obtained using the DFT (Model-AS), ONIOM-ME (Model-ALL), and ONIOM-EE//ME (Model-ALL) methods are compared in Figure 7a. The barrier height was calculated to be 23.9 kcal/mol by Model-AS QM calculations. This was lowered to 20.6 kcal/mol by inclusion of the environmental effect (ONIOM-ME) and to 21.7 kcal/mol after an EE single-point calculation; the surrounding seems to lower the H-abstraction barrier by a few kcal/mol. To identify the factor determining the energy lowering, eq 1 may be rearranged as follows:

$$\begin{aligned} E^{\mathrm{ONIOM}} &= E^{\mathrm{model,QM}} + (E^{\mathrm{real,MM}} - E^{\mathrm{model,MM}}) \\ &= E_{\mathrm{QM}} + E_{\mathrm{MM}} \end{aligned} \tag{3}$$

Using this equation, we analyzed E_{QM} and E_{MM} in the ONIOM-ME energy. The latter term contains the classical interaction energy between the QM and MM regions as well as the energy within the region outside of the QM region. As can be seen in Figure 7b, the QM energy was 23.5 kcal/mol, which is only 0.4 kcal/mol lower than that for Model-AS. By comparison, the relative MM energy at $\mathbf{TS_{2-3}}$ with respect to **2** was −2.9 kcal/mol, which accounts for most of the energy lowering. Further decomposition of E_{MM} showed that the electrostatic and van der Waals components amount to −3.0 and −0.2 kcal/mol, respectively, and the other contributions, i.e., stretching, bending, torsion, and out-of-plane terms, account for 0.2 kcal/mol of E_{MM}.

To gain further insights into the H-abstraction step, the deuterium kinetic isotope effect (^{2}H-KIE) on H-abstraction was evaluated by comparing the rate constants for the reactions of MI and its deuterium-substituted counterpart (D_6-MI). For this purpose, we used the rate constant formula based on the transition-state theory (TST), without and with the Wigner correction for the one-dimensional tunneling effect:

$$k_{\mathrm{TST}} = \left(\frac{k_{\mathrm{B}}T}{h}\right) \exp\left(-\frac{\Delta G^{\ddagger}}{RT}\right) \tag{4}$$

$$k_{\mathrm{Wigner}} = \left[1 + \frac{1}{24}\left(\frac{h\nu^{\ddagger}}{k_{\mathrm{B}}T}\right)^2\right] k_{\mathrm{TST}} \tag{5}$$

ONIOM-ME frequency analyses were performed for the entire Model-ALL system for **2** (side-on) and $\mathbf{TS_{2-3}}$ in **LB** to obtain

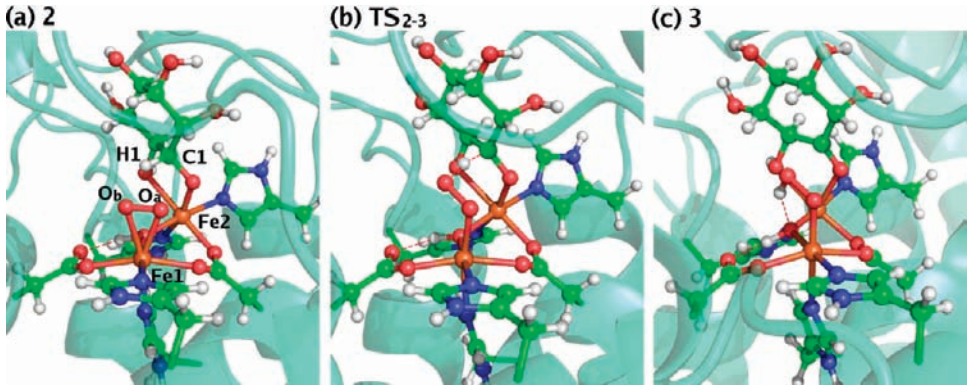

Figure 5. Geometric change during H-abstraction (**LB** state). Detailed geometric parameters can be found in Supporting Information.

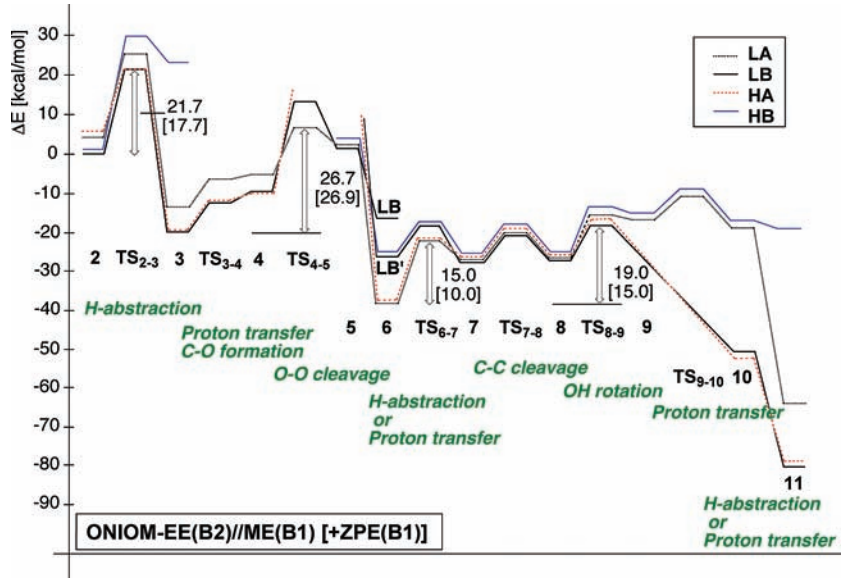

Figure 6. Energy profile obtained from ONIOM-EE(B2)//ME(B1) calculations. The value in square brackets includes ZPE correction.

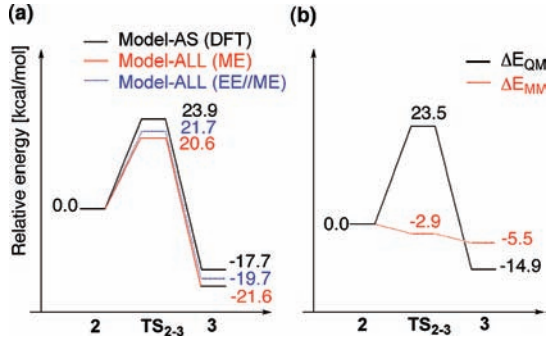

Figure 7. (a) Comparison of H-abstraction barriers for **LB** obtained by several methods. (b) Analysis of the ONIOM-ME barrier.

free energy values and imaginary frequencies that are needed to apply the equations. The ^{2}H-KIE values thus obtained were 6.5 (TST) and 8.8 (Wigner) at 5 °C for **LB**, while the reported experimental value was 8−16.[16] The good agreement between the theoretical and experimental values supports a mechanism in which a hydrogen atom is abstracted from C1 of MI by the (superoxo)Fe(III)Fe(III) intermediate. Furthermore, better agreement of the Wigner corrected value with experiment implies the involvement of tunneling in H-abstraction.

At **3**, the **HB** state was exceptionally high in energy compared with the other states (Figure 6). This can be ascribed to the aforementioned spin localization on C1 (Figure 4), which causes Pauli repulsion against the electrons on Fe2. We also notice that **LA** is more than 5 kcal/mol higher in energy than **LB** and **HA**. This is because the electron reorganization in **LA** leads to lower spin on Fe1 ($\rho_{Fe1}\sim2.8$) at **3**, which thus raises the energy relative to **LB** and **HA** ($\rho_{Fe1}\sim4.2$) (see Figure S1 in Supporting Information).

The distal oxygen of **3** then attacks C1 to form an intermediate **4** containing a C−O bond (Figure 8). Since C1 in **3** does not retain a radical character as discussed earlier, the C1−O part in **3** is better viewed as a carbonyl group. Therefore, this reaction step is described as a nucleophilic attack of $FeOO^-$ on a carbonyl. To facilitate this process, species **3** donates a proton to the oxygen (O_x) of the bridging hydroxide (see arrows in Figure 8) to make $FeOO^-$ that has a higher nucleophilic power than FeOOH or $FeOO^{\bullet}$. A pathway involving direct $^{\bullet}OH$ migration could not be found. Interestingly, this role of hydroxide as a catalytic base is facilitated by nearby Asp253, to which the proton of hydroxide is released (Figure 8). Thus,

(44) The electron that is to shift to O_2 actually has α-spin in the penta-coordinate state, whereas the corresponding electron has β-spin in **2** (**LB**). To avoid confusion due to the insufficiency of broken-symmetry description, we assume a β electon shifts to O_2.

(45) Schöneboom, J. C.; Cohen, S.; Lin, H.; Shaik, S.; Thiel, W. *J. Am. Chem. Soc.* **2004**, *126*, 4017–4034.

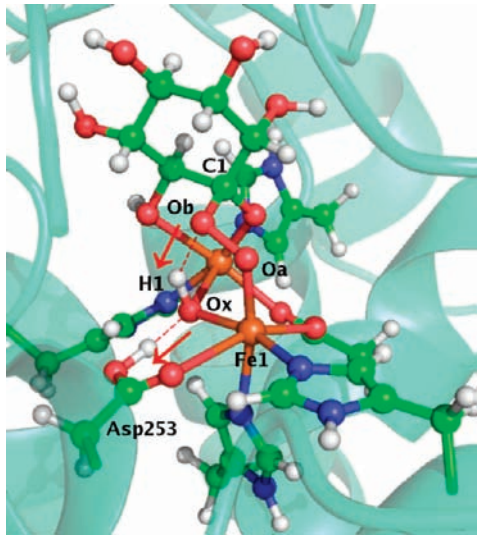

Figure 8. Geometry of species **4**. Red arrows highlight the proton transfers involved when **4** is generated from **3**.

the hydroxide-Asp253 part efficiently acts as a catalytic base in a cooperative manner. While DFT/B1 predicted that **4** would be more stable than **3**, the more reliable ONIOM-EE with B2 (Tables S10 and S11 in Supporting Information) predicts that **3** is a true stable intermediate (while **4** is not). Hence, we propose that the as-yet-uncharacterized intermediate "***H***", which experimentally accumulated after H-abstraction, is **3**.

From **4**, the O−O bond was cleaved homolytically to yield *gem*-diolate **5**. The transition state for O−O cleavage $\mathbf{TS_{4-5}}$ was obtained for **LA** and **LB** en route to **5** (Figure 9a). As we did for the H-abstraction step (Figure 7), we attempted to evaluate the effect of the protein surrounding here again but without success, because optimization of **5** in Model-AS resulted in eventual collapse of the geometry (Table S10 in Supporting Information). This failure can be attributed to the lack of H-bonds with nearby residues in that model. *Thus, the anchoring effect of hydrogen bonding restricts the movement of the substrate in the active site, which appears to be essential for affording the specific catalytic reaction, while preventing any other unwanted reactions.* **LB** becomes less stable than **LA** at $\mathbf{TS_{4-5}}$, which can be understood by the more efficient O−O cleavage in **LA** (Figure S2 in Supporting Information). Assuming that a transition from **LB** to **LA** occurs, the barrier for O−O cleavage is 26.9 kcal/mol at the ONIOM-EE/B2 level with ZPE correction (Figure 6), which is somewhat higher than that obtained with ONIOM-ME/B2 (22.0 kcal/mol). Proton transfer from O_x to the oxygen on C1 then produces species **6** without a barrier. Species **6** has an O−H bond that forms a H-bond with ferryl (Table S5 in Supporting Information). In **6** the ferryl intermediates **LA** and **HA** ($|\rho_{Fe1}| \sim 3.2$) are the most stable states (Figure 5). **LB** has higher energy in **6** than the other states because of the lower spin on Fe2 that developed in the course of reaction (Table S5b in Supporting Information) and its further participation in the reaction after O−O cleavage can be ruled out. However, a more stable high-spin analogue **LB′** with an Fe(III)Fe(III) state having $\rho_{Fe1} \sim 4.2$ as in **HB** was obtained at **6** (Figure S3 and Table S5 in Supporting Information) by changing the orbital occupation of **LB**. The pathway from **LB** to **LB′** was not smooth. These ferric states (**LB′** and **HB**) were less stable than the ferryl states **LA** and **HA** ($|\rho_{Fe1}| \sim 3.2$) at **6**.

The spin population values tell us that, at the stage of **6**, the oxidation state of Fe1 is IV in **LA** and **HA** and III in **LB′** and **HB**.[46] Although the next reaction step is associated with the migration of H1 to O_a in all states, the difference in oxidation state results in a different mechanism for the step from **6** to **7** depending on the spin state. In **LA** and **HA**, the hydrogen atom of the O−H bond in **6** is abstracted by ferryl in **LA** and **HA** (Figure 9b), while proton transfer to oxoferric occurs in **LB′** and **HB**. In both cases, however, Fe(III)OH species **7** is generated (Figure 10a). The barrier for this step at $\mathbf{TS_{6-7}}$ (Figure 9b) was calculated to be 10 kcal/mol in **LA** with ZPE correction (Figure 6). This barrier is not high compared with the other barriers but may nevertheless provide a chance to trap the intermediate **6** experimentally. The C1−C6 bond of **7** can then be cleaved quite readily via $\mathbf{TS_{7-8}}$ to yield **8**. Subsequently, the hydroxyl group on C6 in **8** rotates via $\mathbf{TS_{8-9}}$ to give **9** in **LA** and **HB** so that the O−H bond points to O_b (Figure 9c). In **LB** and **HA** of **9**, however, the proton of the O−H bond is transferred to O_b without any barrier (Figure 6), whereas in **LA** and **HB**, the barrier for the proton transfer is about 7 kcal/mol high. The resultant species **10** is found to convert readily, without a barrier, to **11** (Figure 10) by hydrogen transfer (**LA**) or proton transfer (other states) to the Fe(III)OH. The final species **11** has a water molecule over Fe1 and a D-glucuronate (DG) product over Fe2. In our proposed mechanism, therefore, one of the two oxygen atoms in O_2 (O_a) is converted into water, while the other (O_b) is incorporated into the carboxylate part of DG. This is consistent with the fact that one of the two oxygen atoms in O_2 is incorporated into the substrate (Scheme 1).[9,10]

In the reaction profile, we find a few major barriers at $\mathbf{TS_{2-3}}$, $\mathbf{TS_{4-5}}$, $\mathbf{TS_{6-7}}$, and $\mathbf{TS_{8-9}}$, of which the barrier associated with $\mathbf{TS_{4-5}}$ is the highest (Figure 6). This result suggests that O−O cleavage is the rate-limiting step of the reaction. The ^{2}H-KIE values for the step from **3** (**LB**) to $\mathbf{TS_{4-5}}$ (**LA**) were calculated to be 1.1 (TST) and 1.1 (Wigner); thus, in the rate-limiting step, there should be no marked kinetic isotope effect. Meanwhile, from the result that ^{2}H-KIE on steady-state turnover was close to unity (1.35 ± 0.35), Xing et al. previously concluded that decay of intermediate "***H***", rather than C−H cleavage, is rate-limiting.[16] *Our results support their conclusion and further suggest the main reason for the diminished KIE is the higher barrier for O−O cleavage that constitutes a critical part of the decay process.* At the entrance and exit channels, the **LB** state was found to be stable, while **LA** was the most stable during the middle stage of the reaction. The **HA** state was also stable over almost the entire region of the reaction path. The **HB** state, the second most stable state at **2**, was less stable in most of the steps. Although it is fair to say that the present-day DFT-based approaches are not necessarily so robust as to allow definite conclusions on the responsible spin states in a reaction pathway, a few interchanges of spin states were observed for the MIOX reaction. Involvement of multiple spin states in the reactions of diiron enzymes will remain an open question, and its elucidation presents a new challenge to computational as well as bioinorganic chemistry.

4. Conclusion

We have performed DFT and ONIOM(DFT:MM) calculations on MIOX to understand the nature of its (superoxo)Fe(III)-Fe(III) intermediate **2** and the reaction mechanism. Mechanistic insights obtained by our calculations are consistent with the available experimental data. Furthermore, our studies made quite

(46) Blomberg, M. R. A.; Siegbahn, P. E. M. *Theor. Chim. Acta* **1997**, *97*, 72–80.

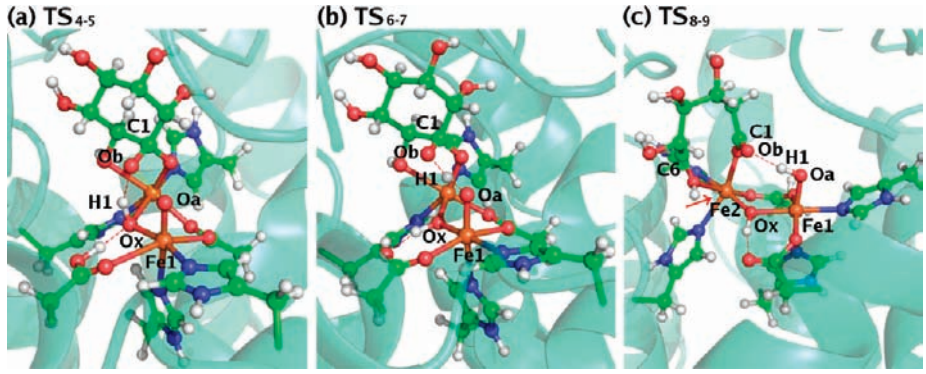

Figure 9. Several key transition states: $\mathbf{TS_{4-5}}$ and $\mathbf{TS_{6-7}}$ in **LA** and $\mathbf{TS_{8-9}}$ in **LB**.

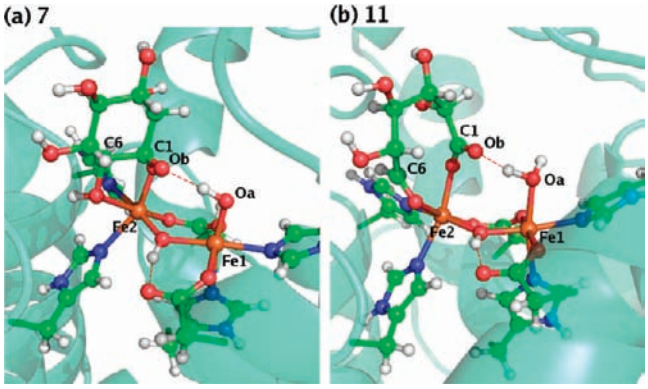

Figure 10. Species **7** and **11**.

a few predictions for the unclear facets of the chemistry of MIOX. The **LB** side-on state is suggested to be the ground state of **2**, in which the two iron sites are antiferromagnetically coupled and the Fe1 and the superoxide site are ferromagnetically coupled. Population and spin density analyses showed that, in this intermediate, charge transfer from Fe1 to O_2 is not complete; nevertheless **2** is capable of abstracting hydrogen from a C−H bond. This was confirmed by the elucidation of the reaction pathway and the calculated deuterium kinetic isotope effect. The experimentally as-yet-uncharacterized intermediate after the H-abstraction step is suggested to be an FeOOH-type intermediate. The protein environment was shown to have a significant effect on the enzyme catalysis. It lowers the barrier for H-abstraction, and the H-bonding anchoring effect that restricts its movement appears essential for the prevention of unnecessary reactions. Homolytic O−O bond cleavage was predicted to be the rate-limiting step of the reaction. This step did not exhibit deuterium kinetic isotope effect, which is consistent with the experimental observation that the deuterium kinetic isotope effect on the steady-state turnover was close to unity. Interestingly, the role of the hydroxide ligand is not only to bridge the two iron ions but also to serve as a catalytic base in some part of the reaction. Thus, it appears that the hydroxide ligand is not an innocent bystander, but a central player in the ingenious proton-shuttle machinery in the MIOX catalysis.

Acknowledgment. We thank Prof. Edward N. Baker for comments on the 2HUO structure. H.H. thanks the JSPS Fellowship for support during his stay at Emory University and the FIFC fellowship for the current support. The authors thank Drs. Marcus Lundberg, Tsutomu Kawatsu, Lung Wa Chung, and Ahmet Altun for helpful discussions. This work was in part supported by a CREST grant in the Area of High Performance Computing for Multiscale and Multiphysics Phenomena from the Japan Science and Technology Agency (JST). The computational resources at the Research Center for Computational Science at Institute for Molecular Science and the Cherry L. Emerson Center for Scientific Computation are gratefully acknowledged.

Supporting Information Available: Complete ref 30, electron reorganization diagrams, AO populations, ESP charges, geometric parameters, group spin populations, relative energies, and XYZ coordinates. This material is available free of charge via the Internet at http://pubs.acs.org.

JA905296W